Chemical Engineering Journal 158 (2010) 623–632

Contents lists available at ScienceDirect

Chemical Engineering Journal

journal homepage: www.elsevier.com/locate/cej

Spatially resolved inline measurement of liquid velocity in trickle bed reactors

Markus Schubert*, Abhishek Khetan[1], Marco Jose da Silva[2], Holger Kryk

Forschungszentrum Dresden-Rossendorf e.V., Institute of Safety Research, P.O. Box 510119, 01314 Dresden, Germany

ARTICLE INFO

Article history:
Received 18 September 2009
Received in revised form 4 February 2010
Accepted 5 February 2010

Keywords:
Capacitance wire-mesh sensor
Trickle bed reactor
Local liquid velocity
Liquid saturation

ABSTRACT

The flow pattern in trickle bed reactors is of an inhomogeneous nature due to a random packing structure. Thus, the local values for liquid phase ratio and velocity are spread over the whole cross-section and a global determination of these values ignores the fact that local phenomena dominate mass and heat transfer and eventually the reactor efficiency. Only if both parameters can be locally quantified, can a realistic picture of the flow fields be drawn.

A new wire-mesh sensor (WMS) setup based on the measurement of electrical permittivity of fluids was used, which can be applied to the packings of porous catalyst particles. A calibration method is proposed to get access to the liquid saturation. Axial velocity distributions are measured via a method based on the spatial tracer pulse time-of-flight between sensing points of two WMSs installed at a distance of few millimeters. The effects of gas and liquid flow rates on local liquid velocities were analyzed.

The proposed technique was validated against liquid collector data, which showed very good agreement. For this purpose, distributions of the volumetric flow rate were calculated by applying the continuity equation to the saturation and velocity data obtained from WMS.

1. Introduction

Packed bed reactors, particularly trickle bed reactors, are widely applied in the petro-chemistry, in wastewater treatment and the biochemical industry, as they are most flexible with respect to varying throughput demands [1]. The trickle bed reactor consists of a random packing of catalyst spheres or cylindrical extrudates. Such configuration is applied to a wide range of operating conditions and sizes making the scale-up and the prediction of the reactor performance very complicated. Due to their inhomogeneous random packing structure, the hydrodynamic parameters, such as local phase holdup and phase velocities, can differ significantly. Mass transfer and reaction rates are directly related to local conditions, and global averaged values fail to provide a realistic picture of the flow fields.

The full characterization of the fluid field requires phase fraction and velocity parameters. While measurement of spatially resolved gas and liquid holdups in trickle beds was made possible with the transfer of tomographic methods mainly from medical into chemical engineering applications, velocity measurement techniques are still quite rare with a degree of success in their application to packings. Two good reviews in the field were published by Chaouki et al. [2] and Boyer et al. [3] where the authors summarized possible tomographic imaging techniques and liquid velocity measurement techniques in gas–liquid and gas–liquid–solid reactors. Particle image velocimetry (PIV) and laser doppler anemometry (LDA) are limited to light-transmissive flows without distinctive solid holdup e.g. in bubble columns [4–7]. To evade this limitation, Therning and Rasmuson [8] applied LDA to measure liquid velocities in a refractive index matched packed bed.

A further technique is thermal anemometry, which was employed to determine fluid velocity by detecting changes in heat transfer from a small electrically heated sensor inside the packing [9]. The electrical current needed to keep the sensor temperature constant indicates the heat transfer, which in turn depends on the fluid velocity. A variety of similar probes were applied to measure local liquid velocities based on heat transfer [10–12]. However, the results do not represent the conditions in the whole cross-section. Furthermore, calibration of such probes to relate the signals directly to local liquid velocities is questionable. One method to get the cross-sectional distribution of the liquid velocity is the numbering-up of local probes. Such an attempt was described by Llamas [13] who installed 87 thermistors at the top of thin steel tubes inserted in the trickle bed reactor cross-section. Due to short lifespan of the thermistors, reliable local liquid velocities could not be obtained.

---

* Corresponding author at: Forschungszentrum Dresden-Rossendorf e.V., Institute of Safety Research, P.O. Box 510119, 01314 Dresden, Germany.
Tel.: +49 351 260 2627; fax: +49 351 260 3651.
E-mail address: m.schubert@fzd.de (M. Schubert).

[1] Permanent address: Department of Mechanical Engineering, Indian Institute of Technology, Kanpur 208016, U.P., India.

[2] Current address: Department of Electrical Engineering (CPGEI), Federal University of Technology Paraná, 80230-901 Curitiba-PR, Brazil.

1385-8947/$ – see front matter © 2010 Elsevier B.V. All rights reserved.
doi:10.1016/j.cej.2010.02.009

Nomenclature

a, b	geometric constants of the sensor
A_{pixel}	pixel area (m^2)
C	capacitance (F)
K	relative electrical permittivity
N_{pixel}	number of pixels
Δs	sensor distance (m)
S.D.	standard deviation
S_{n}	normalized signal
u	superficial velocity (m/s)
v	local velocity (m/s)
V	voltage (V)
$\dot{V}$	flow rate (m^3/s)
V_{R}	reactor volume (m^3)

Greek letters

β	saturation
ε	packing porosity
$\varepsilon_{\mathrm{L,st}}$	static liquid holdup
δ_{L}	reduced liquid saturation
σ	electrical conductivity (S/m)
$\Delta\tau$	pulse peak time-of-flight (s)

Subscripts

dr	drainage
dyn	dynamic
G	gas
j	compartment
log	logarithmic
L	liquid
WMS(s)	wire-mesh sensor(s)
x	sensing point

Superscripts

H	high
L	low
max	maximum
min	minimum

Highly sophisticated and reliable methods for determination of 3D vectorial liquid velocities in multiphase reactors are computer-automated radioactive particle tracking (CARPT) and magnetic resonance imaging (MRI). CARPT is limited to fluidized beds and bubble columns [5,14,15] due to the size of the neutral buoyancy radioactive particle (mm range), which is tracked. MRI has given a unique insight into fluid flow dynamics of opaque systems to quantify the physics and chemistry at different length scales down to 10^{-7} mm [16–19]. The application of MRI in chemical engineering and reactor research is undisputed and the precision is unsurpassed. However, the equipment is expensive, its operation and setup is cumbersome and will not become standard equipment in laboratories and engineering companies in the near future. Furthermore, the application of MRI is limited to only slightly elevated pressures and non-metallic designs.

To summarize, there is still a need for spatially resolved velocity measurement devices that can be easily implemented and that are also economical. The Chemical Engineering Group of ENSIC CNRS in Nancy (Professor Wild) applied the WMS technique developed by Prasser et al. [20], to a trickle bed reactor. They measured liquid fractions and their distribution [21,22], local flow regime transition at individual sensing points of the sensor [23], as well as radial dispersion [24]. However, in their work authors mentioned explicitly that the device used was not applicable to measure liquid velocities and to operate in porous particle media, which are always present in reactive applications. From the electronic point of view the sampling rate was too low (as it took 10–15 s for a whole cross-section scan including 19 × 19 sensing points) to conduct spatially distributed transient studies. Further, the instrument is based on measurement of the electrical conductivity, making it impossible to investigate non-conducting fluids, which are common in most applications of trickle bed reactors such as the synthesis of organic liquids. The general applicability of our capacitance WMS type for hydrodynamic studies of non-conducting fluids was demonstrated by Matusiak et al. [25].

In this paper, a capacitance WMS setup is applied for determination of local liquid velocities and liquid saturation in the whole cross-section of a trickle bed reactor. The axial velocity distribution is measured by the spatial tracer pulse time-of-flight between two corresponding sensing points of the two WMSs installed at a distance of few millimeters. Eventually, both parameters can be considered to validate the system using a segmented liquid collector.

2. Experimental setup

2.1. Trickle bed reactor setup

The experimental setup is shown in Fig. 1. A transparent column (polyvinyl chloride) with an internal diameter of 100 mm was packed up to a height of 135.5 cm with a commercial γ-alumina catalyst packing (KataLeuna GmbH Catalysts) of spherical particles. The catalyst properties are summarized in Table 1. Water and air were used as liquid and gas phase, respectively. The experiments were performed in the recycle-mode with respect to the liquid phase at room temperature and atmospheric pressure conditions. The flow rates were controlled by a pump – with a flow meter operated in a closed loop (LP631, Micropump with Ismatec pump head; Cori-Flow M55-ABD-44V-0-B, Bronkhorst) for the liquid phase and by a flow controller (El-Flow F-202AV-M20-ABD-44 V, Bronkhorst) for the gas phase.

A uniform initial distribution of the liquid phase was realized by different spray nozzles of the full cone type (SSD-VK-5/10/20-60°, Spraying Systems Deutschland GmbH), the operation of which depended on the adjusted flow rates connected to the “L-port” of the distributor plate. The gas was introduced via four holes of 3/8 in. arranged as shown in Fig. 1. Pressure drop along the packing was measured by pressure transducer (Setra, Model: 228-1, 0–69 kPa). A syringe tracer injection port is installed upstream the liquid inlet. Sodium sulfate with a concentration of 0.005 mol/l was used as tracer. Due to low concentration, the effect of tracer on the liquid properties can be neglected. During tracer experiments, the salt-rich liquid at the outlet of the reactor was collected and exchanged by fresh water to prevent any change in the conductivity in the liquid loop.

The trickle bed reactor consists of segments of different lengths to flange-mount the WMS at individual heights of the column. Sealing between the column segments and the sensors was realized by

Table 1
Packing properties.

Parameter	Value
Diameter (mm)	2.5
Bulk density (kg/l)	0.55
Total surface area, BET (m^2/g)	210
Internal porosity	Approx. 0.79[a]
Specific pore volume (ml/g)	Approx. 0.90[a]
Packing porosity	Approx. 0.34[a]

[a] Experimentally determined.

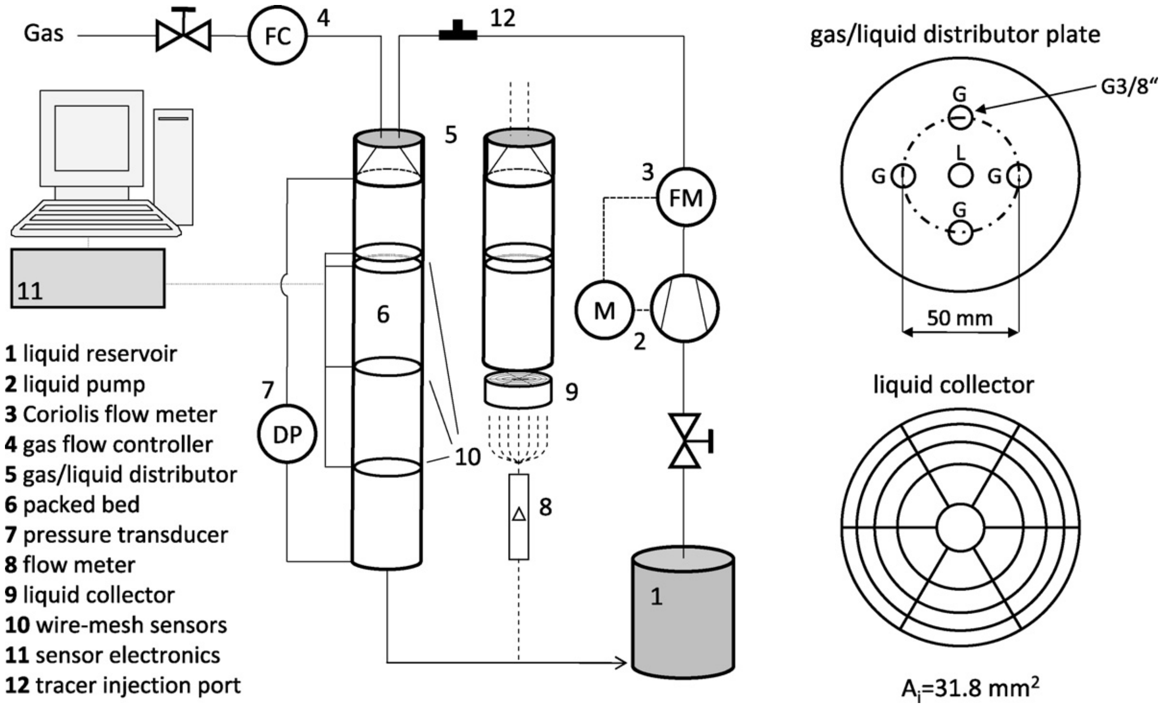

Fig. 1. Experimental trickle bed reactor setup with gas/liquid distributor and liquid collector.

o-rings. Four WMSs were installed in the column at heights 20.4 cm (S1), 22.1 cm (S2), 62.5 cm (S3) and 103.0 cm (S4) downstream the upper end of the packing. For measurement of local liquid velocities, two sensors (twin-sensor: S1 and S2) were installed separated by a spacer segment of 17 mm (see Fig. 2(a)).

Optionally, a liquid collector was installed below the twin-sensor. The collector is divided into 25 compartments of the same area (Fig. 1).

2.2. Wire-mesh sensor

The WMSs are composed of two planes with 16 stainless steel wires of 0.2 mm diameter and 6.0 mm separation in-between them. The distance between planes is 1.5 mm and the wires from different planes run at right angles to one another. This arrangement gives 256 sensing points, thereof 208 inside the circular cross-section of the column. In this way, the wire-mesh subdivides the column cross-section into a number of independent sub-regions, where each crossing point represents one sub-region. For the present WMS, the sampling area of a crossing point represents a square of 0.36 cm^2 (i.e. in-plane wire separation square).

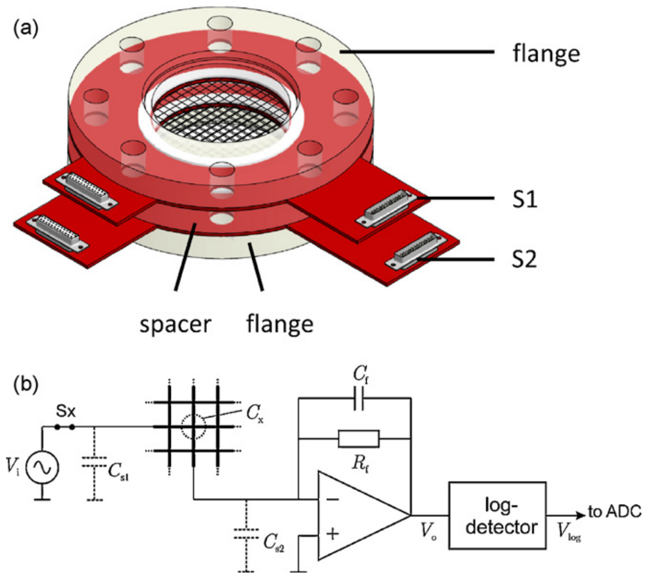

Fig. 2. (a) Wire-mesh twin-sensor and (b) capacitance measuring equivalent circuit for one sensing point.

For spatial analysis, the sensors are mounted in such a way that the sensing points in each sensor have exactly the same spatial coordinates. Since the wires run through the bed, care was taken not to disturb the typical bed structure. Therefore, when building up the reactor, for each single sensor, the part below the sensor was first filled with particles. Next, the sensor was mounted and then particles were carefully placed on top of the wire-mesh to fill up the voidage between the sensing points as well as between the wire-mesh planes.

The WMSs use an alternative current (AC) based method for capacitance measurement [26], where a logarithmic detector scheme is employed for the demodulation of the AC signal [27]. The associated electronics, shown schematically in Fig. 2(b), measures the capacitance between the gaps of all sensing points. Since liquids and gases have different electrical permittivity values and thus produce different capacitances in the sensing points of a WMS, images of liquid distributions can be generated from the measurements of the capacitance. In this study, the WMS signals can be read-out at a maximum frame rate of 1000 fps when all four WMSs operate synchronously.

The general equivalent circuit, which describes the behavior of the fluids in-between the electrodes of a sensing point x is given by a lossy capacitor, i.e. a capacitor C_x in parallel with a resistor. However, for non-conducting fluids or slightly conducting ones (such as tap water used in this study), the conductive effects can be neglected [28].

Assuming the unknown fluid to be represented by a single capacitor, the equivalent circuit for every sensing point (see Fig. 2(b)) shows a logarithmic relation between C_x and the measured voltage $V_{\log,x}$. Further, since C_x and the relative electrical permittivity at the sensing point K_x are directly proportional, Eq. (1) can be applied (for a detailed description see da Silva et al. [27]):

$$V_{\log,x} = a_x \log(K_x) + b_x \tag{1}$$

Unknown constants a_x and b_x depend only on geometric properties of the WMSs and on the modules of the equivalent circuit. These constants were determined by two reference measurements in a column filled with material of known permittivity – in our case air ($K_{\text{air}} = 1$) and water ($K_{\text{water}} = 80.1$), respectively. Eventually, the permittivity at every sensing point K_x can be calculated using Eq. (2):

$$K_x = 10^{(V_{\log,x} - b_x)/a_x} \tag{2}$$

3. Data calibration and analysis method

3.1. Determination of liquid saturation

So far, capacitance WMSs were not applied for liquid saturation measurements in packed beds and trickle bed reactors, respectively. Per definition, liquid saturation, β_{L}, is the liquid volume divided by the extra-granular volume. While conventional drainage measurement method collects free flowing liquid volume of the packing at the outlet which can directly be used to calculate dynamic liquid saturation, $\beta_{\text{L,dyn}}$ (volume of the collected liquid divided by the volume of the reactor and by the porosity), WMS measurements provide permittivity that requires high and low reference measurements (K_x^{H}, K_x^{L}) to calculate the dynamic liquid fraction.

For dynamic liquid saturation in a packing with internal porosity, reference measurements of the flooded packing and of the externally dried packing but with liquid filled internal porosity would be required. However, in practice drained packing is applied for low reference which still contains static liquid, $\varepsilon_{\text{L,st}}$, and eventually results in the reduced liquid saturation, δ_{L}, as defined by Sáez and Carbonell [29] shown in Eq. (3). ε is the packing porosity.

$$\delta_{\text{L}} = \frac{\beta_{\text{L,dyn}}\varepsilon}{\varepsilon - \varepsilon_{\text{L,st}}} \tag{3}$$

In our case, the “high” reference represents the permittivity of the fully saturated packing, $K_x^{\text{H}}(\delta_{\text{L}} = 1)$. Subsequently, the measurement after draining represents the permittivity of the “low” reference, $K_x^{\text{L}}(\delta_{\text{L}} = 0)$. Prior to each experiment, the reactor was operated in the pulse flow mode according to the Kan pre-wetting method to ensure full pre-wetting of the bed [30].

It was shown in electrical capacitance tomography (ECT) studies that different permittivity models exist to relate the permittivity to the reduced liquid saturation [31], which are the parallel model (Eq. (4)), the series model (Eq. (5)), the Maxwell model (Eq. (6)) and the log model (Eq. (7)) as shown in Table 2. The applicability of the models mainly depends on the structure of the system (density, phase permittivity differences, dilution strength, phase dispersion, etc.).

Table 2
Permittivity models.

Model	Equations	
Parallel model	$\delta_{\text{L},x} = \dfrac{K_x - K_x^{\text{L}}}{K_x^{\text{H}} - K_x^{\text{L}}}$	(4)
Series model	$\delta_{\text{L},x} = \dfrac{K_x^{\text{H}}K_x^{\text{L}} - K_xK_x^{\text{H}}}{K_xK_x^{\text{L}} - K_x^{\text{H}}}$	(5)
Maxwell model	$\delta_{\text{L},x} = \dfrac{(2 + K_x^{\text{H}}/K_x^{\text{L}})(1 - K_x/K_x^{\text{L}})}{(1 - K_x^{\text{H}}/K_x^{\text{L}})(2 + K_x/K_x^{\text{L}})}$	(6)
Log model	$\delta_{\text{L},x} = \dfrac{\log(K_x) - \log(K_x^{L})}{\log(K_x^{H}) - \log(K_x^{L})}$	(7)

In the case of a trickle bed reactor, structures are very complex due to the random packing, the non-homogeneous phase distribution and the existence of an internal porosity. Therefore, the best fitting model has to be identified experimentally.

Cross-sectional average values of the reduced liquid saturation, δ_{L}, are calculated with Eq. (8) taking the reduced pixel area at the outer ring of the cross-section into account.

$$\delta_{\text{L}} = \frac{\sum_x (A_{\text{pixel},x}\delta_{\text{L},x})}{\sum_x (A_{\text{pixel},x})} \tag{8}$$

When the packing porosity and static liquid holdup are known, Eq. (3) can be re-arranged and dynamic liquid saturation, $\beta_{\text{L,dyn,WMS}}$, can be calculated from reduced liquid saturation (Eq. (10)):

$$\beta_{\text{L,dyn,WMS}} = \delta_{\text{L}}\frac{\varepsilon - \varepsilon_{\text{L,st}}}{\varepsilon} \tag{9}$$

For calibration of the WMS data, additional drainage experiments were performed for a wide range of gas and liquid superficial velocities and dynamic liquid saturation, $\beta_{\text{L,dyn,dr}}$, was calculated from the drained liquid volume, $V_{\text{L,dr}}$, based on Eq. (10):

$$\beta_{\text{L,dyn,dr}} = \frac{V_{\text{L,dr}}}{V_R\varepsilon} \tag{10}$$

Fig. 3 shows the parity plot comparing the WMS dynamic liquid saturation results, $\beta_{\text{L,dyn,WMS}}$, where different permittivity models are applied with those from drainage experiments, $\beta_{\text{L,dyn,dr}}$. It can be concluded that the parallel model should be applied for calculation of the liquid saturation based on capacitance measurements. However, the derivation from exact parity could be related to the fact that the permittivity of the packing is not considered explicitly in the models but interferes in a more complex manner. Similar deviating calibration curves were obtained in ECT studies, for example shown by Liu et al. [32]. Eventually, a linear calibration equation can be derived (see Fig. 3). As no reconstruction algorithm (algebraic reconstruction technique, linear back projection, etc.) is necessary to obtain the saturation distribution in the cross-section, this calibration equation can be applied to every pixel, as well.

It should be mentioned, that the relative error (Eq. (11)), which is dependent on the packing porosity and the static liquid holdup,

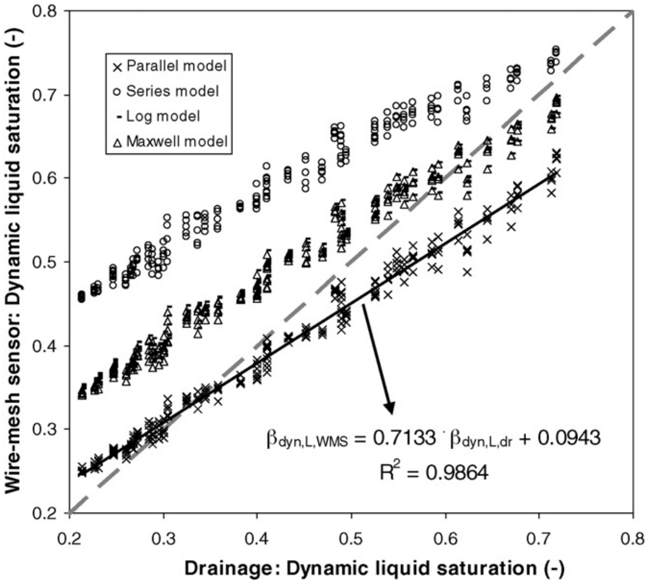

Fig. 3. Dynamic liquid saturation parity plot for different permittivity models.

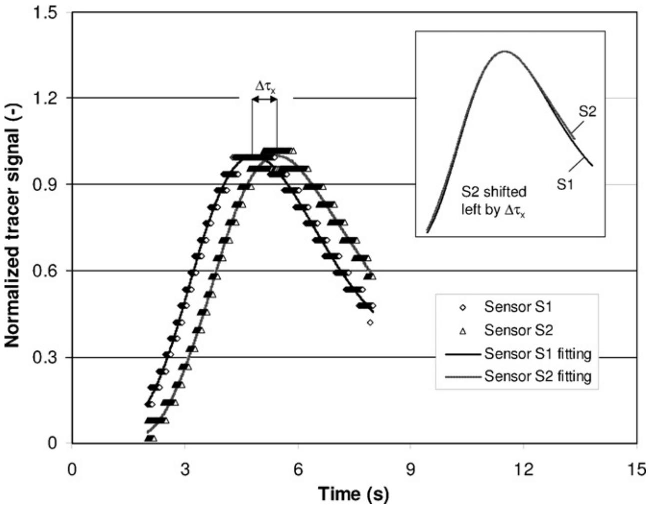

Fig. 4. Tracer signals S1 and S2 obtained for $u_L = 0.49$ cm/s and $u_G = 2.12$ cm/s at pixel position {07;11}.

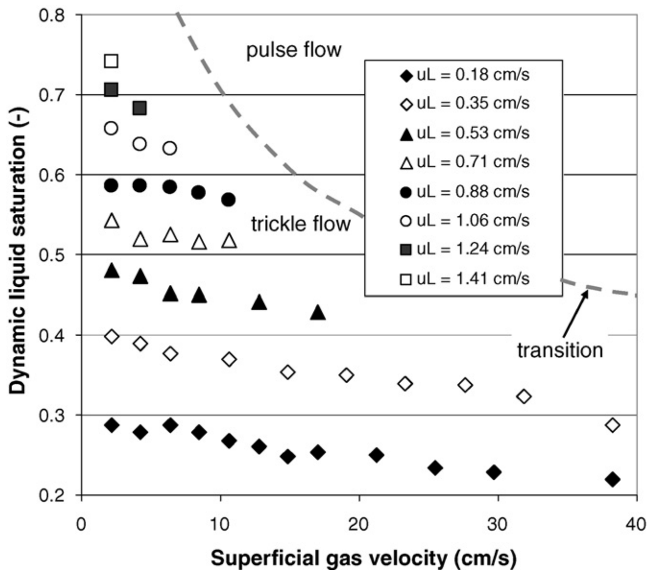

Fig. 5. Effect of superficial gas and liquid saturation on dynamic liquid saturation.

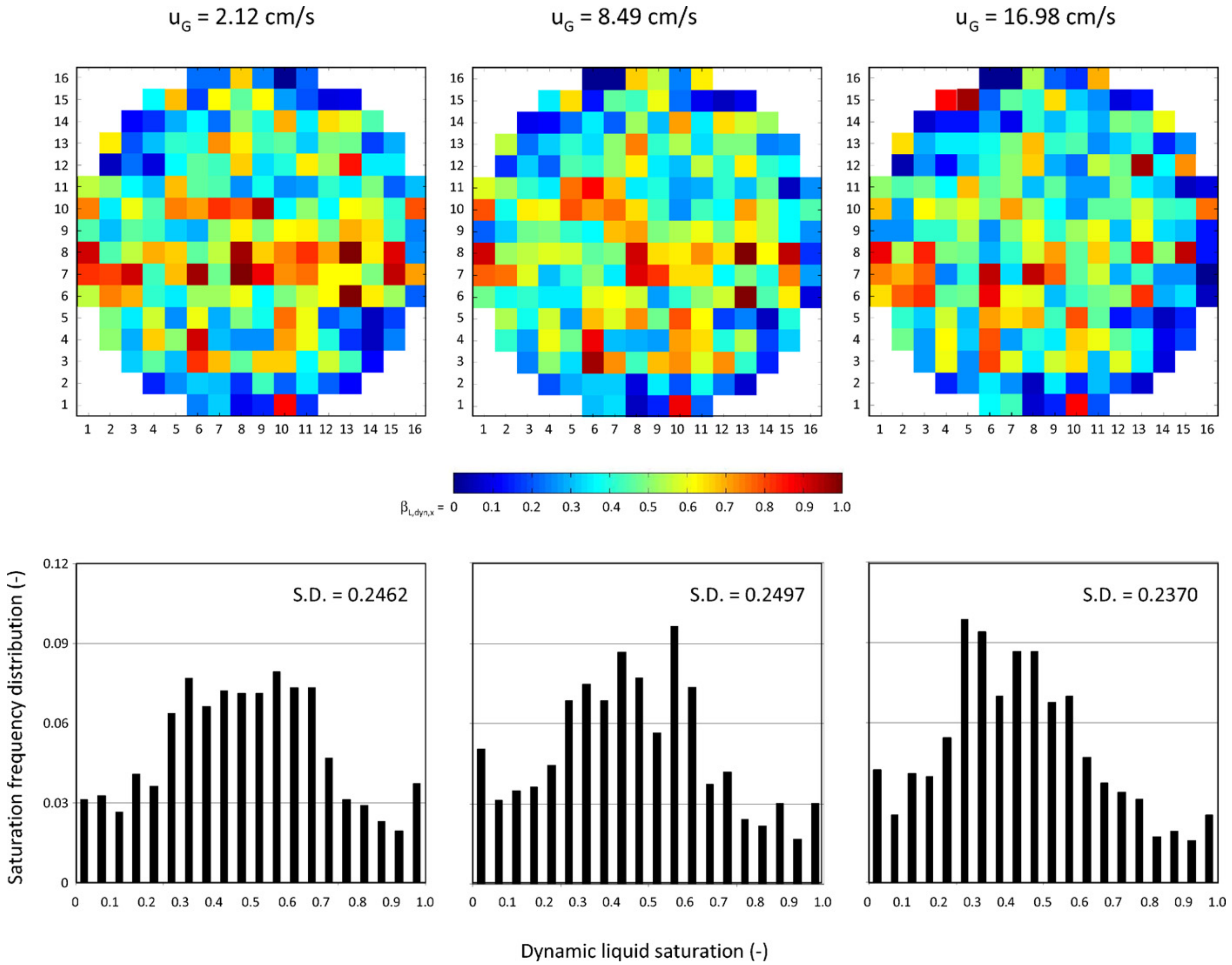

Fig. 6. Effect of superficial gas velocity on dynamic liquid saturation and corresponding frequency distribution of the local dynamic liquid saturation ($u_L = 0.53$ cm/s).

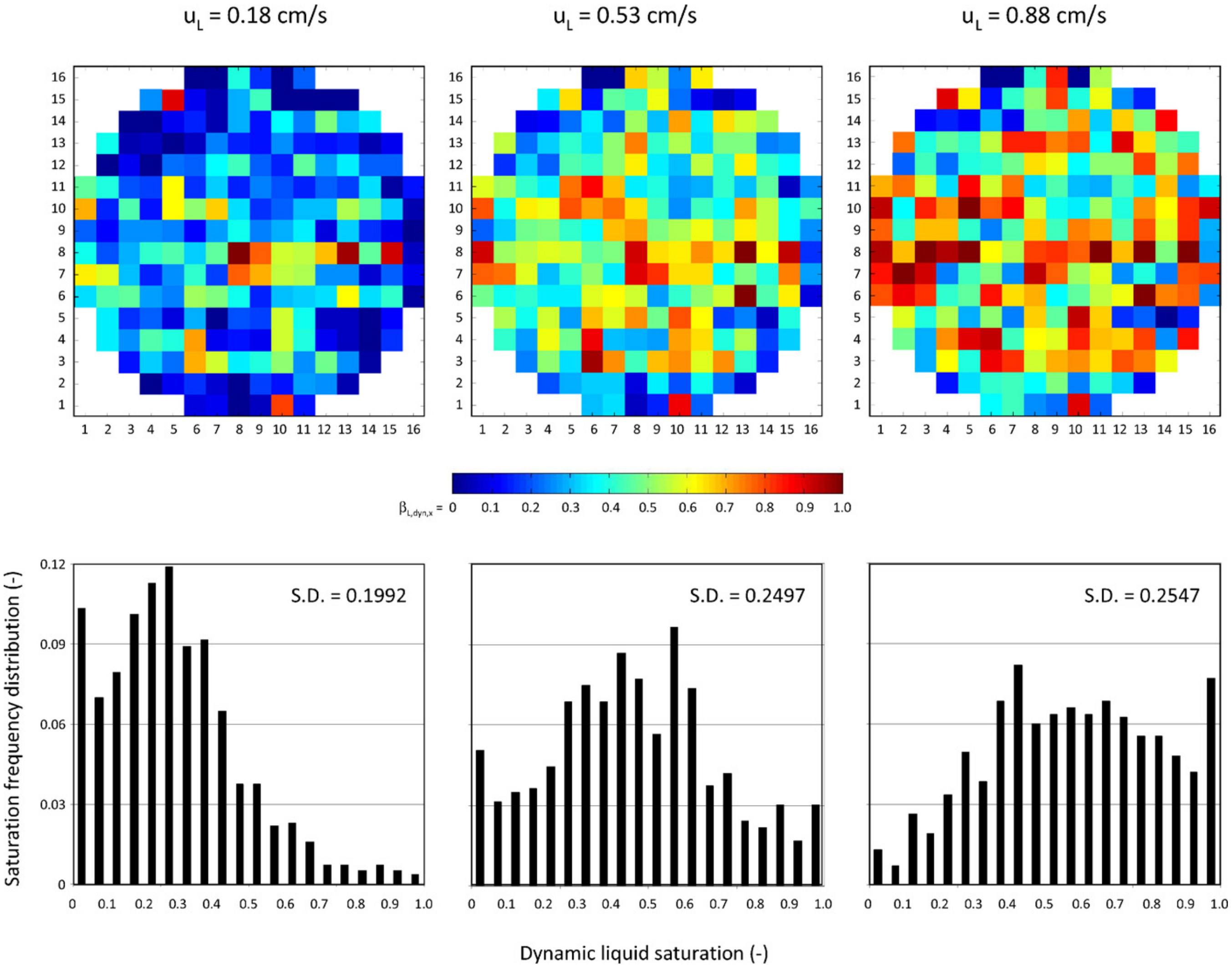

Fig. 7. Effect of superficial liquid velocity on dynamic liquid saturation and corresponding frequency distribution of the local dynamic liquid saturation ($u_G = 8.49$ cm/s).

can be large if the reduced liquid saturation from WMS measurement, δ_L, is considered as a dynamic liquid saturation, $\beta_{L,dyn,WMS}$. This fact should be considered for all tomographic studies where media with internal porosity are applied because the static liquid fraction and internal liquid in the pores cannot be separated and determined experimentally. Relative errors (Eq. (11)) increase with smaller porosity and higher static liquid fractions:

$$\text{error} = \left| \frac{\beta_{\mathrm{L,dyn,WMS}} - \delta_{\mathrm{L}}}{\beta_{\mathrm{L,dyn,WMS}}} \right| = \frac{\varepsilon_{L,\mathrm{st}}}{\varepsilon - \varepsilon_{\mathrm{L,st}}} \tag{11}$$

In our case, based on correlations proposed by Sáez and Carbonell [29], the static liquid holdup was determined to be 0.0495. This would result in a relative error of 14.3% if the reference volume were not reduced by the static liquid volume.

3.2. Determination of local liquid velocity

Although the circuit of the capacitance WMS was conceived and implemented to measure only the capacitance, the introduction of conducting fluids (such as saline water) will produce changes in the measured $V_{\log}$. In that case, Eq. (1) is no longer valid and the fluids in-between the sensing point must be described as lossy dielectric, i.e. the equivalent circuit is formed by a capacitor (linked with fluid permittivity) and a resistor (linked with fluid conductivity).

It was shown by da Silva [33], for conductivity values higher than 500 μS/cm, the resistive part of the complex impedance becomes dominant and the response of $V_{\log}$ becomes logarithmic dependent on the conductivity (Eq. (12)):

$$V_{\log,x} \sim \log(\sigma_{\mathrm{L},x}) \tag{12}$$

Utilizing this behavior, conductivity tracers can be applied to measure the velocity based on the tracer pulse time-of-flight between the planes of two stacked WMSs. It is worth to note that for velocity measurements one is not interested in the absolute value of conductivity or permittivity. In fact, the passage of tracer through each plane must be correctly recognized and the time delay between the planes has to be quantified. Corresponding pixel signals of sensors S1 and S2 were normalized according to Eq. (13):

$$S_{n,x} = \frac{10^{V_{\log,x}(\sigma_{\mathrm{L},x})} - 10^{V_{\log,x}^{\min}}}{10^{V_{\log x}^{\max}} - 10^{V_{\log x}^{\min}}} \tag{13}$$

The local liquid velocity was based on the time-of-flight of a tracer pulse peak, which considered the distance between both WMSs (see Eq. (14)):

$$v_{\mathrm{L},x} = \frac{\Delta s}{\Delta \tau_x} \tag{14}$$

It should be mentioned that axial dispersion and tortuous liquid pathways cannot be detected. However, due to low distance between both WMSs, these effects were neglected. Fig. 4 shows the tracer pulses at both sensors S1 and S2. Shifting the normalized tracer signal of sensor S2 by $\Delta\tau_x$ to the left side demonstrates the consistent shape of the response curve, which indicates a negligible dispersion within the short distance.

4. Results and discussion

4.1. Liquid saturation measurement

Fig. 5 represents the dynamic liquid saturation in the cross-section averaged over all four sensors. The dynamic liquid saturation deviations between all sensor planes were negligible. Increases in the superficial gas velocity resulted in a slight reduction of the values for the dynamic liquid saturation. Contrary to this effect, the saturation is strongly sensitive to the superficial liquid velocity. It can be concluded that the saturation behavior based on the WMS data is in line with the results shown in the literature (e.g. shown by Al-Dahhan and Dudukovic [34] and Aydin and Larachi [35]).

The effects of the superficial gas and liquid velocities on the spatial distribution of the saturation values are discussed below. In Figs. 6 and 7, the distribution of the dynamic liquid saturation in the cross-section is depicted for sensor S4 at 103.0 cm downstream the upper end of the packing. However, the normalized frequency distribution of the local dynamic liquid saturation for the corresponding couples of superficial gas and liquid velocities are calculated by consideration of the sensing points of all four WMS (4 × 208) to increase the statistical certainty.

The cross-sectional images in Fig. 6 confirm the low effect of the gas flow rate on the cross-sectional averages dynamic liquid saturation. It becomes more obvious, if we consider the frequency distribution of the local data for the dynamic liquid saturation. The mode of the distribution is not affected by the increasing gas flow rate. However, the peak plateau of the distribution at the lowest gas flow rate acuminates slightly with higher values.

The gas phase hardly has an effect on the mean value of the dynamic liquid saturation, as channel flow is reduced towards higher gas flow rates (see pixels in rows 7 and 8 in Fig. 6).

The color-scale distribution images in Fig. 7 highlights clearly the effect of the superficial liquid velocity on the dynamic liquid saturation. The frequency distribution changes from right-skewed to left-skewed frequency distributions with increasing superficial liquid velocity. Furthermore, the standard deviation increases monotonically.

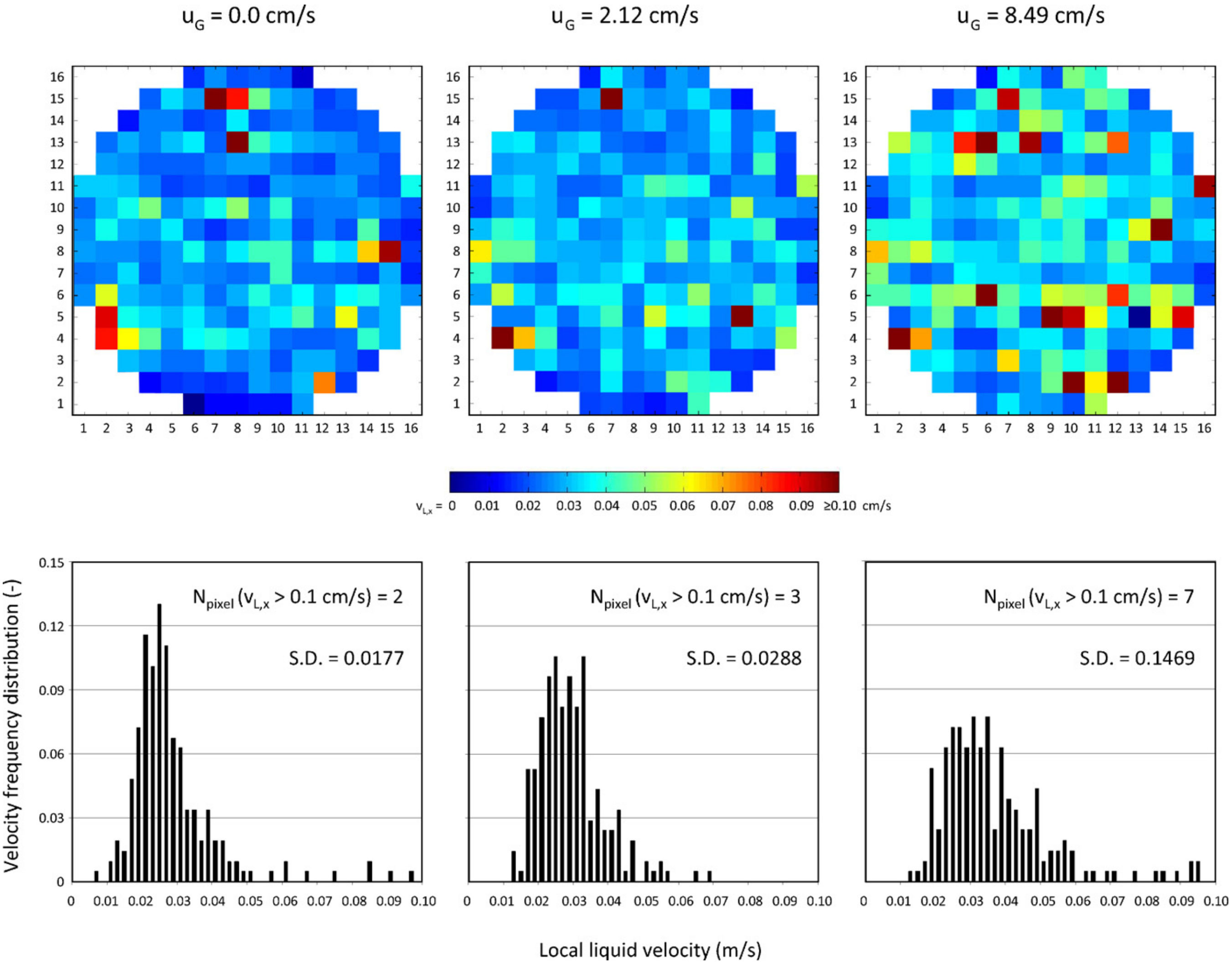

Fig. 8. Effect of superficial gas velocity on liquid velocity distribution and corresponding frequency distribution of the local liquid velocities (u_L = 0.71 cm/s).

4.2. Liquid velocity measurement

The main focus of our study was the measurement of spatially resolved liquid velocities. The distribution of the liquid velocities was determined by injecting 10 ml of saline tracer, which had a conductivity of 0.7 S/m. Subsequent to the tracer injection, the signals of both stacked sensors S1 and S2 (twin-sensor) at every sensing point were recorded with a frequency of 1000 Hz. The local velocities were calculated according to the introduced routine above. Fig. 8 shows the liquid velocity distribution in the cross-section and the corresponding frequency distribution of the local liquid velocities for a superficial liquid velocity of 0.71 cm/s at different superficial gas velocities. The color scale indicates the local liquid velocities from 0 to 0.1 cm/s.

It is obvious that the velocities at many local positions increase with increasing gas flow rate even if the velocity at some pixels positions remains constant. The packing structure was not modified from experiment to experiment. It is well-known that the liquid distribution and flow in the voidage is very stable in the trickling flow regime. The preferred flow paths persist even if the gas velocity increases. This behavior is strongly pronounced at positions with high velocities (see pixels {15;7} and {4;2} in Fig. 8). Such pixels can also be an indication for higher local void fractions (inhomogeneities) as higher porosity directly results in higher flow rates.

A more detailed view on the velocity measurements can be obtained from statistical analysis. The corresponding frequency distributions for the local velocities are shown below the cross-sectional images. The mode values of the local velocities increase with increasing gas flow rate from approximately 0.025 cm/s for liquid only flow to approximately 0.035 cm/s for a gas superficial velocity of 8.49 cm/s. Furthermore, the distributions become clearly wider for higher gas flow rates. It should be mentioned that pixels with velocities higher then 0.1 cm/s are not considered in the frequency distribution for ease of comparison. The number of such pixels, $N_{\text{pixel}}(v_{L,x} > 0.1\text{ cm/s})$, increases with augmentations in the gas flow rate, which indicates a higher number of flow channels.

The effect of the superficial liquid velocity on the liquid velocity distribution in the cross-section and the corresponding normalized frequency distribution of the local liquid velocities for a constant superficial gas velocity of 2.12 cm/s at different superficial liquid velocities are shown in Fig. 9. Increasing the superficial liquid velocity shifts the frequency distribution to higher values. Particularly, this effect is obvious at the highest superficial liquid velocity of $u_L = 1.06$ cm/s.

It should be mentioned that all experiments were performed in the trickle flow regime. The algorithms used to extract the velocity information require stable flow conditions. For other flow conditions, e.g. pulse flow, further developments in data/image

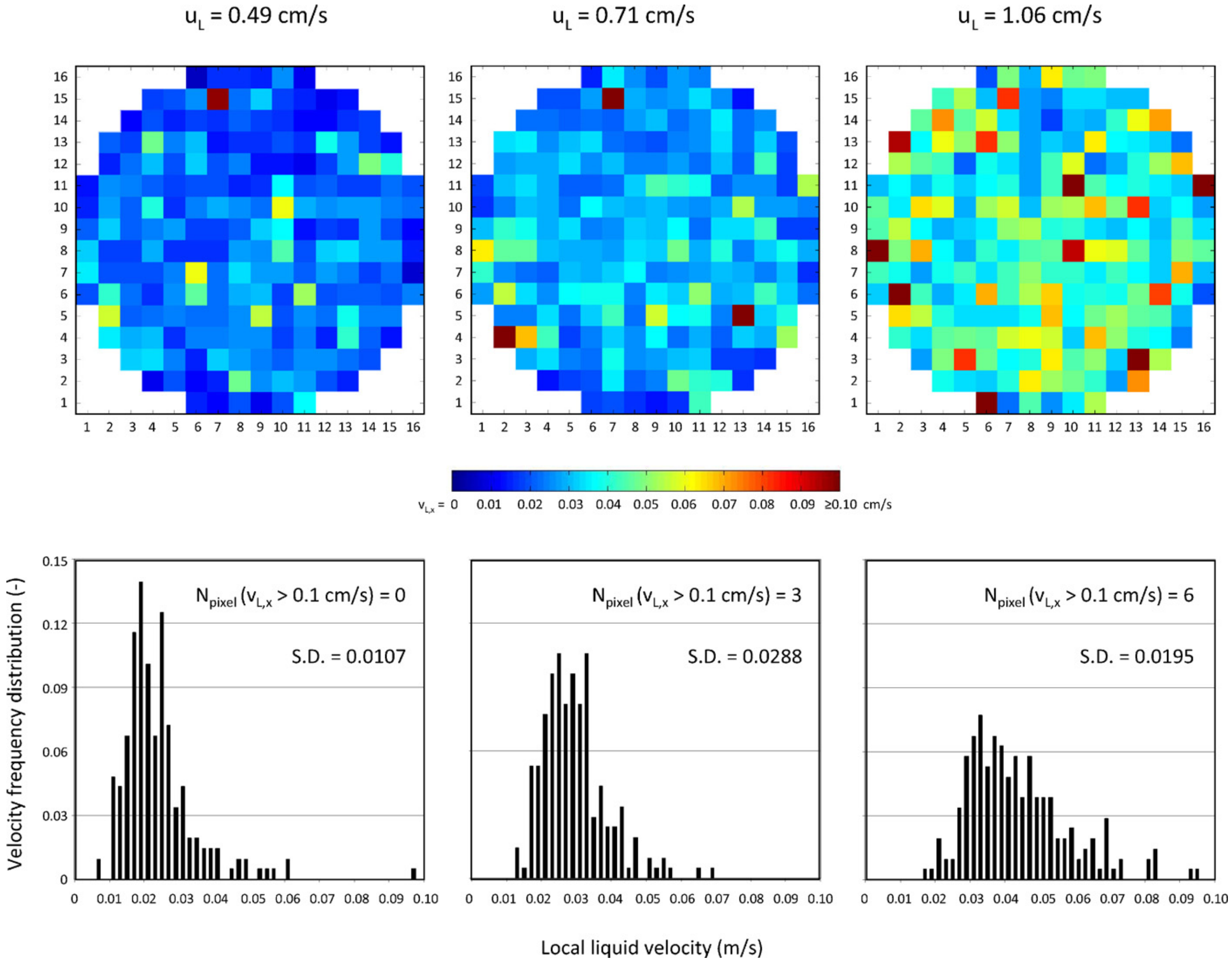

Fig. 9. Effect of superficial liquid velocity on liquid velocity distribution and corresponding frequency distribution of the local liquid velocities ($u_G = 2.12$ cm/s).

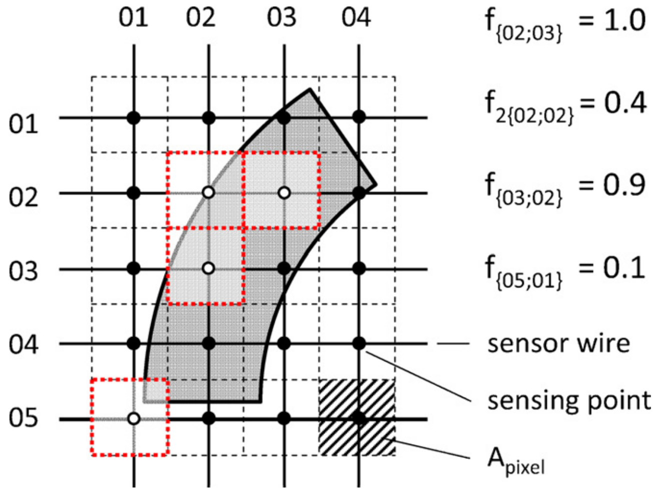

Fig. 10. Definition of area-weighting factors for sensing points within the compartment.

processing are necessary since the natural pulses may mask the tracer pulses.

4.3. Validation of wire-mesh sensor data

To validate the WMS measurements of local liquid velocities and liquid saturation, experiments were performed using the liquid collector below the twin-sensor. The liquid flow rates were obtained by successively collecting the liquid volume in all 25 compartments over a period of 1 min. It was proven that the flow was steady state over the whole collection period as the average flow rate in the compartments reproduced the adjusted flow rate with a deviation of less than 1%.

For the same steady operating conditions, the volumetric liquid flow rates can also be calculated according to the application of the continuity equation to the WMS liquid saturation and velocity measurement. Thus, local saturation and velocity data obtained from subsequent WMS measurements at steady state were applied to Eq. (15) together with the area-weighting factor of every sensing point f_x that contributes to compartment j of the collector.

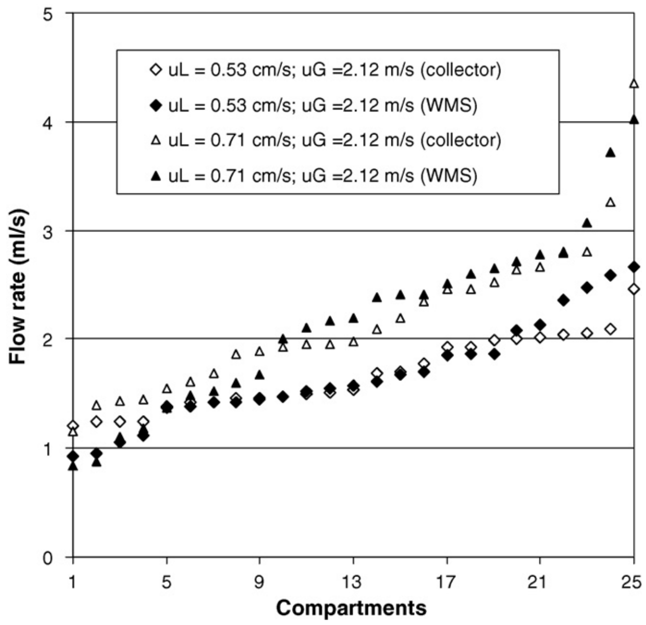

Fig. 11. Comparison of compartments flow rates from collector and wire-mesh sensor (sorted by increasing flow rate).

$$\dot{V}_{\mathrm{L},j} = \sum_{x} \beta_{\mathrm{L,dyn},x} v_{\mathrm{L},x} f_x A_{\mathrm{pixel},x} \varepsilon \tag{15}$$

Fig. 10 shows schematically how the area-weighting factors for all sensing points of the compartment are defined by applying Eq. (16) with a standard pixel area $A_{\mathrm{pixel}} = 0.36\,\mathrm{cm}^2$ (pixel area at the outer ring of the cross-section is lower depending on its position):

$$f_x = \frac{A^{*}_{x(\in j)}}{A_{\mathrm{pixel},x}} \tag{16}$$

We observed from saturation measurements at different heights that the distribution in the cross-section changed, while statistical values (frequency distribution, average value and standard deviation) remained nearly constant. As the collector could not be installed directly below the twin-WMS, a straight correlation from the defined compartment of the sensor to the corresponding compartment of the collector below was not possible. However, the obtained flow rates in the compartments were re-arranged in increasing order and plotted in Fig. 11.

The corresponding curves (collector and WMS) are in an excellent agreement and demonstrate the applicability of the combined velocity/saturation measurement in porous media using WMSs to analyze spatial distributed flow rates.

$$\dot{V}_{\mathrm{L}} = \sum_{j} \dot{V}_{\mathrm{L},j} \tag{17}$$

Furthermore, the total sums of the individual compartment flow rates calculated from WMS measurements (Eq. (17)) were equal to the adjusted liquid flow rates (less then 0.6% error), which is very satisfying taking into account that errors consist of contributions from both the saturation and the velocity measurements.

5. Conclusion

A new high-speed capacitance-based WMS system was successfully applied to a packing of porous particles that enables access to the dynamic liquid fractions and to the real liquid velocities in trickle bed reactors simultaneously for all sensing points of the whole cross-section.

Experiments that studied the influence of different superficial gas and liquid velocities on local dynamic liquid saturations and velocities were performed using a trickle bed reactor at pilot plant scale. Increasing the gas flow rate results in higher velocities at many positions of the cross-section even if the velocity at some positions remains constant. The number of positions with increasing liquid velocities grows with higher gas flow rate. The frequency distributions of the local liquid velocities indicate that augmentations of the gas flow rate resulted in right-shifted frequency distributions. Same trends were observed for the effect of the liquid flow rate.

The local analysis of the liquid velocity highlighted that, once a stable trickle flow is developed, preferred flow paths persist even if the gas velocity increases as long as the packing structure is the same.

In order to validate the WMS measuring approach, local flow rates based on WMS measurements of velocities and dynamic liquid saturations were calculated and compared to data from local flow rate measurements using a segmented liquid collector mounted below the twin-WMS.

Even if phase fraction measurements were shown only with an air/water system, as our WMS technique is based on capacitance (admittance) measurements, it can be applied for non-conductive (e.g. organic) liquids as well. To perform velocity measurements which require conductive tracers, so-called conductivity improvers can be added to the non-conductive organic liquid as shown by Hamidipour et al. [36].

Therewith, this technique can result in a powerful and cost-efficient measuring device e.g. for industrial hydrotreating trickle bed reactors. Further advantage of our capacitance WMS is its applicability to measure quantitatively the liquid fraction in industrial packings of porous particles, which is not the case for conductivity WMSs.

Acknowledgement

The authors would like to acknowledge KataLeuna GmbH Catalysts, Germany for providing the catalyst particles.

References

[1] M.P. Dudukovic, F. Larachi, P.L. Mills, Multiphase catalytic reactors: a perspective on current knowledge and future trends, Catal. Rev. Sci. Eng. 44 (2002) 123–246.

[2] J. Chaouki, F. Larachi, M.P. Dudukovic, Noninvasive tomographic and velocimetric monitoring of multiphase flows, Ind. Eng. Chem. Res. 36 (1997) 4476–4503.

[3] C. Boyer, A.-M. Duquenne, G. Wild, Measuring techniques in gas–liquid and gas–liquid–solid reactors, Chem. Eng. Sci. 57 (2002) 3185–3215.

[4] Z. Liu, Y. Zheng, PIV study of bubble rising behavior, Powder Technol. 168 (2006) 10–20.

[5] J. Chen, A. Kemoun, M.H. Al-Dahhan, M.P. Dudukovic, D.J. Lee, L.-S. Fan, Comparative hydrodynamics study in a bubble column using computer-automated radioactive particle tracking (CARPT)/computed tomography (CT) and particle image velocimetry (PIV), Chem. Eng. Sci. 54 (1999) 2199–2207.

[6] R.F. Mudde, J.S. Groen, H.E.A. van den Akker, Liquid velocity field in a bubble column: LDA experiments, Chem. Eng. Sci. 52 (1997) 4217–4224.

[7] A.A. Kulkarni, J.B. Joshi, V.R. Kumar, B.D. Kulkarni, Application of multiresolution analysis for simultaneous measurement of gas and liquid velocities and fractional gas hold-up in bubble column using LDA, Chem. Eng. Sci. 56 (2001) 5037–5048.

[8] P. Therning, A. Rasmuson, LDA measurements of liquid velocities in a refractive index matched packed bubble column, Chem. Eng. Sci. 60 (2005) 717–726.

[9] J.G. Boelhouwer, H.W. Piepers, A.A.H. Drinkenburg, Particle-liquid heat transfer in trickle-bed reactors, Chem. Eng. Sci. 56 (2001) 1181–1187.

[10] A.V. Sapre, D.H. Anderson, F.J. Krambeck, Heater probe technique to measure flow maldistribution in large scale trickle bed reactors, Chem. Eng. Sci. 45 (1990) 2263–2268.

[11] C. Marcandelli, G. Wild, A.S. Lamine, J.R. Bernard, Measurements of local particle-fluid heat transfer coefficient in trickle-bed reactors, Chem. Eng. Sci. 54 (1999) 4997–5002.

[12] D. Borremans, S. Rode, G. Wild, Liquid flow distributions and particle-fluid heat transfer in trickle bed reactors: the influence of periodic operation, Chem. Eng. Process. 43 (2004) 1403–1411.

[13] J.D. Llamas, Etude expérimentale de la maldistribution des fluides dans un réacteur à lit fixe en écoulement co-courant descendant de gaz et de liquide, Ph.D. Thesis, L'Institut National Polytechnique de Lorraine, 2009.

[14] F. Larachi, J. Chaouki, G. Kennedy, M.P. Dudukovic, Radioactive particle tracking in multiphase reactors: principles and applications, in: F. Larachi, J. Chaouki, M.P. Dudukovic (Eds.), Non-Invasive Monitoring of Multiphase Flows, Elsevier Science B.V., 1997, pp. 335–406.

[15] M.S. Fraguío, M.C. Cassanello, F. Larachi, S. Limtrakul, M.P. Dudukovic, Classifying flow regimes in three-phase fluidized beds from CARPT experiments, Chem. Eng. Sci. 62 (2007) 7523–7529.

[16] L.F. Gladden, M.D. Mantle, A.J. Sederman, Quantifying physics and chemistry at multiple length-scales using magnetic resonance techniques, Adv. Chem. Eng. 30 (2005) 63–135.

[17] L.F. Gladden, M.D. Mantle, A.J. Sederman, Magnetic resonance imaging of catalysts and catalytic processes, Adv. Catal. 50 (2006) 1–75.

[18] L.F. Gladden, L.D. Anadon, C.P. Dunckley, M.D. Mantle, A.J. Sederman, Insights into gas–liquid–solid reactors obtained by magnetic resonance imaging, Chem. Eng. Sci. 62 (2007) 6969–6977.

[19] M.H. Sankey, D.J. Holland, A.J. Sederman, L.F. Gladden, Magnetic resonance velocity imaging of liquid and gas two-phase flow in packed beds, J. Magn. Reson. 196 (2009) 142–148.

[20] H.M. Prasser, A. Böttger, J. Zschau, A new electrode-mesh tomograph for gas–liquid flows, Flow Meas. Instrum. 9 (1998) 111–119.

[21] J.D. Llamas, C. Pérat, F. Lesage, M. Weber, U. D'Ortona, G. Wild, Wire mesh tomography applied to trickle beds: a new way to study liquid maldistribution, Chem. Eng. Process.: Process Intensification 47 (2008) 1765–1770.

[22] J.D. Llamas, F. Lesage, G. Wild, Influence of gas flow rate on liquid distribution in trickle-beds using perforated plates as liquid distributors, Ind. Eng. Chem. Res. 48 (2009) 7–11.

[23] J.D. Llamas, F. Lesage, G. Wild, Local liquid saturation measurements inside a trickle bed reactor operating near the transition between pulsing and trickling flow, Chem. Eng. Sci. 62 (2007) 7225–7232.

[24] J.D. Llamas, F. Lesage, G. Wild, Radial dispersion in trickle-bed reactors: comparison between sock and dense loadings, Chem. Eng. Sci. 65 (2010) 538–541.

[25] B. Matusiak, M.J. da Silva, A. Romanowski, U. Hampel, Measurement of dynamic liquid distributions in a fixed bed using electrical capacitance tomography and capacitance wire mesh sensor, Ind. Eng. Chem. Res. (2010), http://dx.doi.org/10.1021/ie900988f.

[26] W.Q. Yang, T.A. York, New AC-based capacitance tomography system, IEE Proc. Sci. Meas. Technol. 14 (1999) R1–R13.

[27] M.J. da Silva, E. Schleicher, U. Hampel, Capacitance wire-mesh sensor for fast measurement of phase fraction distribution, Meas. Sci. Technol. 18 (2007) 2245–2251.

[28] M.J. da Silva, U. Hampel, Field-focusing imaging sensor for fast visualization of multiphase flows, Meas. Sci. Technol. 20 (2009) 104009.

[29] A.E. Sáez, R.G. Carbonell, Hydrodynamic parameters for gas-liquid cocurrent flow in packed beds, AIChE J. 31 (1985) 52–62.

[30] K.-M. Kan, P.F. Greenfield, Multiple hydrodynamic states in cocurrent two-phase downflow through packed beds, Ind. Eng. Chem. Proc. Des. Dev. 17 (1978) 482–485.

[31] T.R. McKeen, T.S. Pugsley, The influence of permittivity models on phantom images obtained from electrical capacitance tomography, Meas. Sci. Technol. 13 (2002) 1822–1830.

[32] G. Liu, J.-A. Lan, Y. Cao, Z. Huang, Z. Cheng, Z. Mi, New insights into transient behaviors of local liquid-holdup in periodically operated trickle-bed reactors using electrical capacitance tomography (ECT), Chem. Eng. Sci. 64 (2009) 3329–3343.

[33] M.J. da Silva, Impedance Sensors for Fast Multiphase Flow Measurement and Imaging, TUD Press, Dresden, 2008.

[34] M.H. Al-Dahhan, M.P. Dudukovic, Pressure drop and liquid holdup in high pressure trickle-bed reactors, Chem. Eng. Sci. 49 (1994) 5681–5698.

[35] B. Aydin, F. Larachi, Trickle bed hydrodynamics and flow regime transition at elevated temperature for a Newtonian and a non-Newtonian liquid, Chem. Eng. Sci. 60 (2005) 6687–6701.

[36] M. Hamidipour, F. Larachi, Z. Ring, Monitoring filtration in trickle beds using electrical capacitance tomography, Ind. Eng. Chem. Res. 48 (2009) 1140–1153.